Proceedings of the Tenth Asian Congress of Fluid Mechanics
17-21 May 2004, Peradeniya, Sri Lanka

IN-VITRO STUDY OF A BIO-CENTRIFUGAL VENTRICULAR ASSIST DEVICE MODEL

K. S. Ong, L. P. Chua and S.C.M. Yu
School of Mechanical and Production Engineering, Nanyang Technological University, Singapore

ABSTRACT: The paper presents the flow field of the Bio-centrifugal pump with particular emphasis on the flow inside the clearance gap between the rotating impeller and stationary casing, and the passages between impeller blades. No vortex formation is observed within the clearance gap. A strong washout mechanism is found in the gap around the starting of the splitter plate of the double volute. This has further suggested that thrombus formations are minimal in the gap and hence the pump is able to function nominally efficient as compared to other centrifugal pumps. On the other hand, recirculation flows are found to appear in the impeller passages due to the splitter plate. However, their existences are in short time interval such that their effect on the blood should be neglected.

1. INTRODUCTION

Hemolysis prone to occur when erythrocytes are subjected to high shear forces especially at the region of sudden flow directional change. Thrombus formation could happen in low velocity or recirculating regions. Therefore, different aspects of investigation are necessary for the eventual development of centrifugal blood pumps for long-term and implantable cardiac assist device [1]. In general, most of the measurements have been limited due to technical difficulties so that little has been revealed of the flow within blade passages and small gap between the impeller shroud and the pump casing [2]. This could be understood from the fact that intrusive measurements are extremely difficult and non-intrusive measurements are limited by the optical access. The focus of this study is to understand the flow field inside the impeller passages and the clearance gap using non-intrusive technique. Low velocity and recirculation flow regions could then be identified. Shear stress level has also been estimated from the velocities obtained.

2. MATERIALS AND METHODS

The prototype bio-centrifugal VAD designed by Professor K. Akamatsu (Kyoto-NTN MSCBP) [3] consists of two volutes in the pump casing with a splitter plate that starts from $\theta = 180^o$ is shown in Figure 1. The fluid at the upper half of the pump ($\theta = 0^o$ to 180^o) is discharged through the outer volute and the fluid at the lower half of the pump ($\theta = 180^o$ to 360^o) through the inner volute. The VAD model in this investigation is five times scaled up based on dimensional analysis and flow conditions (i.e. the head coefficient $(\frac{H}{\rho N^2 D^2})_{prototype} = (\frac{H}{\rho N^2 D^2})_{\mathrm{mod}\,el}$ and flow coefficient $(\frac{Q}{ND^3})_{prototype} = (\frac{Q}{ND^3})_{\mathrm{mod}\,el}$) to facilitate the measurements [4,5]. The pump casing and the front shroud of the impeller are made of acrylic and highly polished to boost up the optical access.

The impeller comprises 16 radial blades, with the entrance angle, β_1 of 0^o and the trailing edge angle, β_2 of 90^o. The blades are sandwiched by two disks to form an impeller with two shrouds. Figure 2 shows the schematic geometry of the impeller. The radial extent of each blade begins at the inner radius of 65mm and ends at the outer radius of 125mm. Four selected blades, which are 90^o apart, has larger thickness to accommodate the fastening screws of the front shroud.

Blood analogue, used as the fluid medium has similar viscosity (0.34×10^{-3} kg/ms) and density ($1060 kg/m^3$) as blood. Moreover, the refractive index of the blood analogue is similar to the pump casing

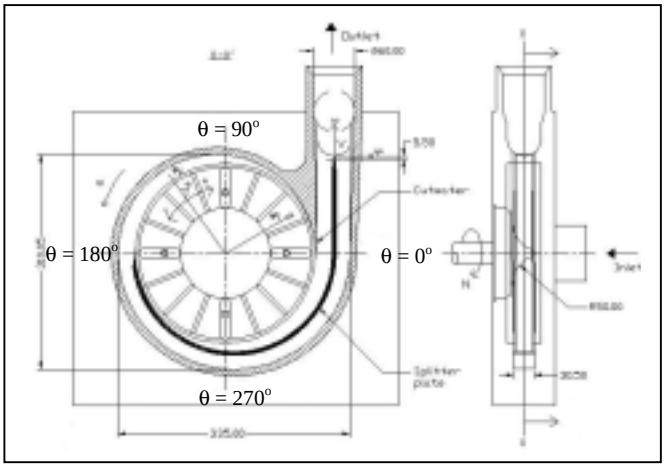

Fig. 1: Schematic sectional view of the bio-centrifugal

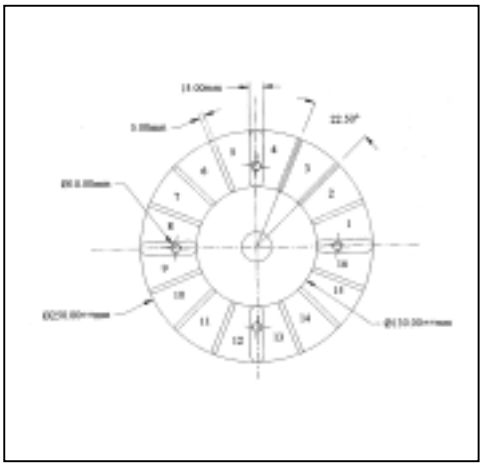

Fig. 2: The detail dimension of the impeller

and impeller shroud material. This could make the non-intrusive measurement possible by transmitting the laser through the pump casing and impeller without optical obstruction.

A four beams two components fiber optic, together with 0.5W Argon air-cooled laser LDV system of TSI Incorporated, operating in a backward scattered mode is used to measure the respective velocity. The natural contaminants inside the blood analogue appear to be sufficient to produce high validation data rate. The laser beams transmit from the front of the pump, through the transparent front shroud of the impeller. The measurement volume of the laser is placed within the passage of the impeller.

The ensemble-averaged velocities are collected with 2000 sample data points and the sampling duration is set at 20 second. The velocities within the gap (1mm) between the impeller shroud and the pump casing are measured at seven different radii and angular locations at the interval of 5 degree. Tangential and radial direction components are measured simultaneously. Then the resultant velocity magnitude, V and the flow direction, θ_r are obtained by combining them. The velocities within the impeller passages are measured with the assist of encoder and the rotating machinery resolver module (RMR). The shear stress distribution is then estimated by using the velocities obtained with the expression of $\tau_{r\theta} = \mu(\frac{1}{r}\frac{\partial u}{\partial \theta} + \frac{\partial v}{\partial r} - \frac{v}{r})$, where $\tau_{r\theta}$ is the shear stress in N/m^2, μ is the viscosity of the working fluid, which is 0.34 x 10^{-3} Kg/ms, v is the tangential velocity in m/s, u is the radial velocity in m/s, θ is the angle in radian and r is the radial position in m.

The pump runs at 200 rpm and delivered about 80 l/min of fluid at the pressure of 32 mmHg during the velocity measurements. These are equivalent to about 5 l/min of output and at the pressure of 100 mmHg in the prototype. Figure 3 shows performance curves for the 5:1 model with blood analogue, prototype with Glycerol solutions and prototype with bovine blood. It is found that the performance curve of the scaled up pump model follows closely to those of the prototype using Glycerol solution and bovine blood.

3. RESULTS AND DISCUSSION

Figure 4 shows the resultant velocity vectors in the clearance gap. The vector magnitude, V is represented by the vector length with a scale factor of Grid Units/Vector magnitude equals to 10. The tail of the vector is positioned at the point where measurements were taken. It could be observed that the flow is generally in tangential direction with slightly tilted towards the eye of the impeller, except those in the

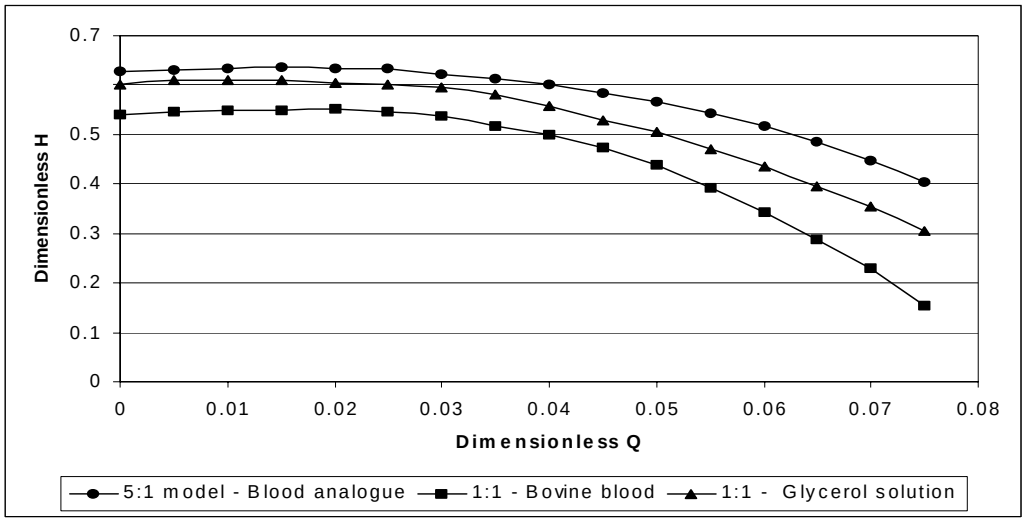

Fig. 3: Pump performance comparison between the model and the prototype

region from $\theta = 120^o$ to $\theta = 220^o$ (around the region of the starting of the splitter plate), which are more towards the eye of the impeller. The higher flow rate in this region has formed a washout mechanism that is required and is essential to flush the blood in the clearance gap to the eye of the impeller and reenter the impeller passages and the volute. Figure 5 shows the schematic of the blood flow path in the VAD. Blood that stagnated in the gap could cause thrombus formation [6]. It could also be observed that there are no traces of flow reversal or vortex formed in the gap.

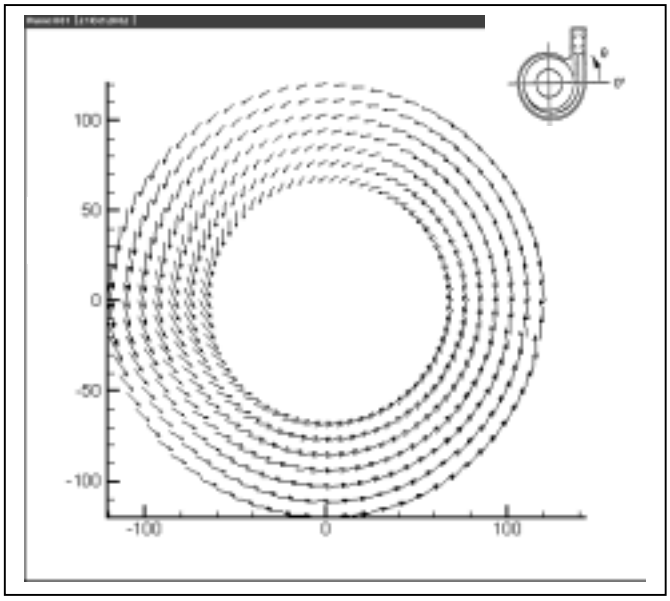

Fig. 4: Velocity distribution in the gap between the impeller shroud and the pump

The high flow rate at the region around the starting of the splitter plate is due to more fluid left the impeller passages as a result of through-flow characteristic. This could be observed in Figure 6, which shows the mean value of the angle-resolved relative velocities in the impeller passages. The vector length represents the magnitude by a scale factor of Grid Units/Vector magnitude equals to 7. On approaching

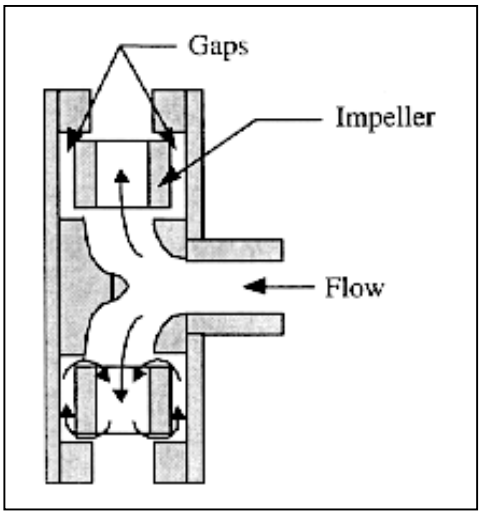

Fig. 5: Schematic of the blood flowing path at inlet, impeller passages and the gap

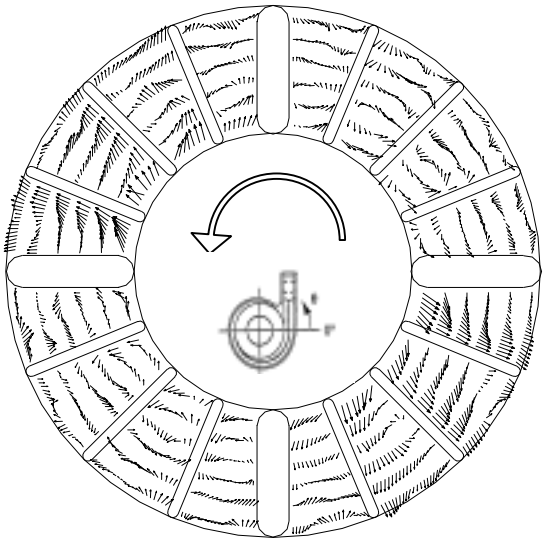

Fig. 6: Angle-resolved velocity distribution within the impeller passages

the starting point of the splitter plate, the flow in the impeller passages is blocked again, and the through-flow characteristic disappear. The fluid that is entering the gap is reduced gradually and flows less in radial direction.

The flow in the impeller passages could be broadly divided into four quadrants separated by the thicker blades. The flow in quadrant 1 is nearly similar to those in quadrant 3 while the flows in quadrant 2 are nearly the mirror image of those in quadrant 4. The flow in quadrant 1 and 3 are restricted and partially become reversing flow, subsequently formation of vortices. The cutwater at $\theta = 0^o$ has blocked the fluid to enter the volute partially in quadrant 1. While the splitter plate is responsible for restricting the flows at quadrant 3. The recirculation flows increase the risk of hemolysis and thrombus formation due to expected high shear stress and stagnation flow. However, these high shear stress regions should not be the critical regions to cause hemolysis and consequently thrombus formation. The impeller turns continuously

at the speed of 2000 rpm in the prototype. The recirculations in quadrant 1 and 3 are transient and will disappear, then transform to washout flow when these passages enter the region of quadrant 2 and 4 where the through-flow characteristics exist. Note that the flow in quadrant 1 and quadrant 3 are not completely blocked, some of the flows appear to 'squeeze' into the discharge volute at the suction side of the blades.

Obvious through-flow characteristics could only be observed in quadrant 2 and quadrant 4. The magnitudes of the velocities inside the passages are generally higher than those in quadrant 1 and quadrant 3. The through-flow characteristics are essential as it could flush the blood to the volute and thus prevent the erythrocytes from being trapped in the impeller passages and over exposed to high shear stress. The impeller is turning at 200 rpm in the scaled-up model and ten times higher in the prototype, which is 2000 rpm. Therefore, it takes only 0.0075 second for an impeller passage which is carrying vortices in quadrant 1 or 3 to reach quadrant 2 or 4 to form the through-flow characteristics. Note that, the flow in quadrant 2 and quadrant 4 follow the blade geometry with small departure from the blade curvature at the suction side of the blades. The flow skews toward the front face of the blades (pressure side).

Figure 7 shows the shear stress distributions within the impeller passages. In general, the shear stresses are found to be low and fall within the range of 0.02-0.6 N/m^2 (0.45–13.56 $dyne/cm^2$ in the prototype). However, some high stresses could hit as high as 0.9 N/m^2. The high stress is found in the region where the recirculation existed. However, these high shear stress regions should not be the critical regions to cause immediate hemolysis and consequently thrombus formation. The occurrence of hemolysis highly depends on the exposing time of erythrocyte to high shear stress and the condition of the contact surface. The short high shear exposure time for the erythrocyte due to the through-flow characteristics in quadrants 2 and 4 would keep them substantial, direct and immediate disruption on the erythrocyte by high shear could be prevented. It was reported by Treichler [4] that blood would remain healthy by exposing up to 1500 $dyne/cm^2$ for less than 10^2 second. However, in fact, the high shear stress is increasing the speed of aging of the erythrocyte.

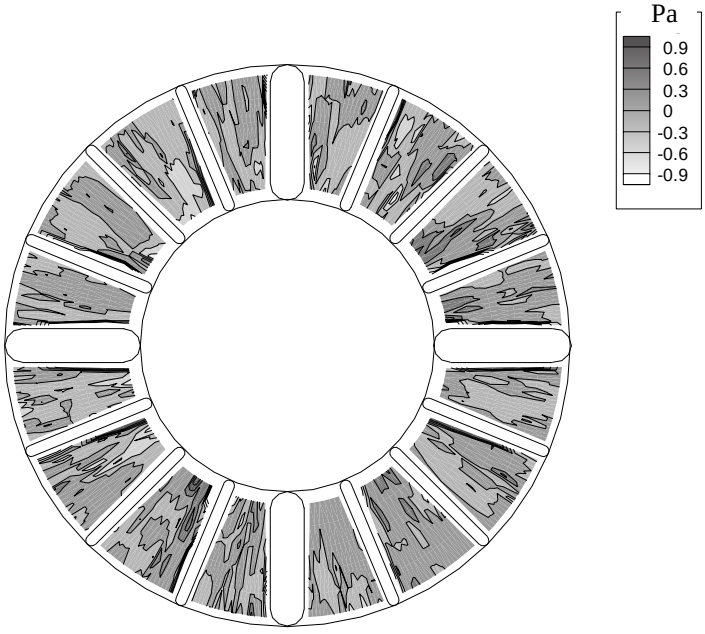

Fig. 7: Shear stress distribution within the impeller passages

4. CONCLUSION

The results show that no recirculation flows appear in the gap but they do appear in some of the impeller passages. The resultant velocity vector in the gap indicated a good washout of blood appeared around the region of the starting of the splitter plate. The washout mechanism would flush the fluid in the gap towards the eye of the impeller. The double-spiral volute design has significantly affected the fluid flow and the shear stress distribution in the clearance gap. The location of the splitter plate and the cutwater are decisive on the washout mechanism of the pump. On the other hand, the splitter plate has influenced the flow in the impeller passages and caused reversing flow. Based on the finding in this investigation that aforecited, the Kyoto-NTN MSCBP could be predicted to have a higher merit of pump performance with has relatively low level of hemolysis and thrombus formation.

REFERENCES

[1] Day SW, McDaniel JC, Wood HG. Particle image velocimetry measurements of blood velocity in a continuous flow ventricular assist device. *ASAIO Journal*, 2001, **47**, 406-411.

[2] Treichler J, Rosenow SE, Damm G. A fluid dynamics analysis of a rotary blood pump for design improvement. *Artif Organs*, 1993, **17(9),** 797-808.

[3] Akamatsu T, Nakazeki T, Itoh I. Centrifugal blood pump with a magnetically suspended impeller. *Artif Organs*, 1992, **16(3),** 305.

[4] Chua LP, Ong KS, Yu SCM. Gap velocity measurements of a blood pump model. *Artif Organs*, 2002, **26(8)**, 682-694.

[5] Chua L P and Akamatsu T. Measurements of gap pressure and wall shear stress of a blood pump model. *Medical Engineering and Physics*, 2000, **22**, 175-188.

[6] Wakisaka Y, Taenaka Y, Araki K. Effects of self washout structure on the antithrombogenicity and the hemolytic properties of a centrifugal pump. *Artif Organs*, 1997, **21(2)**, 148-153.

Proceedings of the Tenth Asian Congress of Fluid Mechanics
17-21 May 2004, Peradeniya, Sri Lanka

PERFORMANCE OF BATTERY-CHARGING WIND TURBINE DEVELOPED BY THE NERD CENTRE

M. Narayana
National Engineering Research & Development Centre of Sri Lanka, 2P/17B Industrial Estate, Ekala, Ja-Ela, Sri Lanka, Fax: ++94-11-7354597,E-mail: nerdc@sri.lanka.net

A G T Sugathapala
Mechanical Engineering Department, Faculty of Engineering, University of Moratuwa, Moratuwa, Sri Lanka. Fax: ++94-11-2647622, E-mail: thusitha@mech.mrt.ac.lk

ABSTRACT: A number of wind-turbine-generators installed in various parts of Sri Lanka have not been functioning at efficiency levels expected from them. This study was carried out to predict the performance of a wind turbine-generator, and to check whether the failures are really due to mismatch of the wind rotor and the generator. A two-bladed small-scale wind turbine-generator has been developed for battery-charging applications. For a wind-turbine-generator to maximise its energy output, the characteristic performance of the electric generator coupled to it should match with the characteristic performance of wind rotor. The performance of the wind-rotor developed for this study is theoretically predicted by considering the vortex system of the wind-rotor by using blade element theory and momentum theory, where the geometrical parameters (β, C) of the existing blade are used.
According to the final results of this study, the performance of the wind-rotor is not properly matching with the permanent-magnet generator used with it. The performance curves of the wind-rotor and the generator were used in determining the curve of real power output of entire system at different wind speeds.

1. INTRODUCTION

In certain rural areas of Sri Lanka, battery-charging-wind-turbine has been identified as a viable off-grid power system, instead of costly electrification, for homes. In this context, National Engineering Research & Development Centre (NERDC) of Sri Lanka has developed a two-bladed, small-scale wind-turbine-generator for battery-charging applications.

This simple unit consists of a two-bladed wind-rotor directly coupled to a permanent-magnet generator. An inclined-hinged-tail vane is installed for both self-orientation of the wind-rotor to wind direction and for power control at wind speeds greater than the rated wind speed.
A number of wind-turbine-generators have been installed in the country, but most of them are not performing to the expectations. This study was carried out to predict the performance of a wind-turbine-generator, and to check whether the failures are due to their mismatch. To maximise energy output, the characteristic performance of the electric generator should be matched with that of the wind rotor.

2. CHARACTERISTICS OF THE WIND ROTOR

In the analysis of the characteristic performance of a wind-rotor, the main parameters are thrust force on the rotor, torque generated by the rotor, and rotational speed of the rotor. These parameters should be found at different values of wind speeds in order to analyse the characteristic performance of the wind-rotor. This is very important when it has to be coupled to an electric generator. A wind-rotor, in general, is designed so that optimum energy conditions are satisfied at a given specific tip-speed ratio. But in practise wind rotors do not always function at optimum conditions. It may run at various other tip-speed ratios.
Power output of this wind-turbine-generator was evaluated for different wind speeds. The main objective here is to theoretically find out the C_p values for different λ_0 values of the NERDC wind-rotor. Geometrical parameters of the rotor are presented in table 1. Performance of the existing wind-rotor can

be analyzed by using the blade element theory (BET) and momentum theory (MT). This rotor consists of two blades with Profile NACA 4415[2]. The radius of the rotor is 1105 mm, and the hub radius is 105 mm.

Table 1: Geometrical parameters of 2-bladed wind rotor at NERDC

Section	Radius (mm)	Chord length (mm)	Blade angle, β (degrees)
1	155	189.2	22.0
2	255	177.7	19.5
3	355	166.2	17.1
4	455	154.7	14.7
5	555	143.2	12.3
6	655	131.7	9.8
7	755	120.2	7.4
8	855	108.7	5.0
9	955	97.2	2.6
10	1055	85.7	0.2

2.1 Blade Element Theorems and Momentum Theorem

Energy extracted from the wind is transmitted through the rotor in the form of torque, and the air is acted upon with a reactive torque that makes the wake to rotate opposite to the rotor motion. This implies that the downstream air consists of rotational kinetic energy, which is not included in the axial momentum theory. Indeed, this energy component represents a part of energy in air, which could not be absorbed by the rotor. Therefore, a more realistic value for C_{pmax} can be derived by the inclusion of wake-rotational effect [1].

It should be noted that the wake-rotational effect is the main case for low C_p values in low-speed wind-rotors. These rotors impart higher reactive torques on the wind, than high-speed rotors, which result in higher wake-rotations leading to higher losses. Figure 1 shows the basic configuration of the flow through a wind-rotor with wake-rotation. The rotor speed is denoted by ω, and rotational speed of the wake given by Ω varies along the radius r.

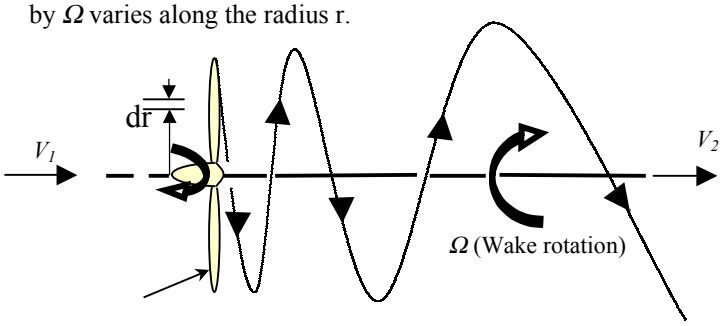

Figure 1: Flow behind the rotor with wake-rotational effect

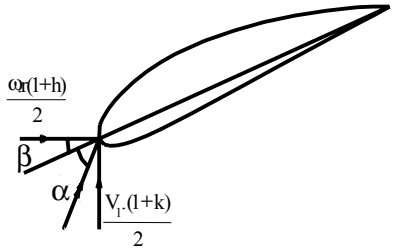

Figure 2: Velocity diagram of a blade element

As seen from figure 1:

Downstream of the rotor, the rotational speed of the wind flow is Ω.

Hence, $\Omega = h\omega$,

The axial speed through the rotor can be derived.

Let, $V_2 = k\,V_1$

where, V_1 - wind speed, h - radial flow interference factor and k - axial flow interference factor.

As seen from figure 2:

$$\phi = \alpha + \beta \quad (1)$$

$$\cot\phi = \frac{U}{V} = \frac{\omega.r.(1+h)}{V_1.(1+k)} \quad (2)$$

$$= (\omega.r/V).\ (1+h)/(1+k)$$

$$= \lambda.\ (1+h)/(1+k) \quad (3)$$

2.2 Aerodynamic Performance

The performance of the wind rotor is theoretically predicted by considering the wake-rotation of the wind-rotor by using blade element theory and momentum theory, where the geometrical parameters *(*β - blade angles*, l* – chord lengths of each blade elements) of the existing blade are used. The characteristic performance of a wind-rotor is usually given by the variation of power coefficient (C_p) with respect to tip-speed ratio (λ_0).

Calculation of axial thrust and torque:
Considering the blade element theory, axial thrust *dF* is given by:

$$dF = b.d.F_v = \frac{\frac{1}{2}.\rho.l.W^2.b.C_l.\cos(\phi-\varepsilon).dr}{\cos\varepsilon} \quad (4)$$

Aerodynamic torque, *dM*, is given by:

$$dM = r.b.dF_u = \frac{\frac{1}{2}.\rho.l.r.W^2.C_l.\sin(\phi-\varepsilon).dr}{\cos\varepsilon} \quad (5)$$

where, C_l - coefficient of lift, C_d - coefficient of drag, $\tan\varepsilon = C_d/C_l$
ρ - air density , b - number of blades of wind rotor
and W - wind speed relative to the wind rotor, l – chord length of blade element

The above two values, dF and dM, can be determined by the general dynamics theory. Consider the axial momentum of the flow through the annulus:

Thrust = (rate of mass flow, m, through the element) x (change in the axial velocity).

Then, axial thrust, $dF = \rho.\ \pi.r.dr.V_1^2.(1\text{-}k^2)$ (6)

Aerodynamic torque,

$$dM = \rho.\pi.\ r^2.\ dr.\ V_1.\ (1+k)\ \Omega$$

$$= \rho.\pi.r^3.dr.\omega.V_1.(1+k).(h\text{-}1) \quad (7)$$

Comparing the expression for *dF* derived by blade elementary theory with that derived by momentum consideration given in equations (4) and (6 leads to, after substituting for W,

$$C_l.b.l = \frac{2\pi.r.V_1^2.(1-k^2).\cos\varepsilon}{W^2.\cos(\phi-\varepsilon)} = \frac{8\pi.r.(1-k).\cos\varepsilon.\sin^2\phi}{(1-k).\cos(\phi-\varepsilon)}$$

Similarly, comparing dM given in equations (5) and (7),

$$C_l.b.l = \frac{2\pi.r.V_1.(1+k).(h-1).\cos\varepsilon}{W^2.\sin^2(\phi-\varepsilon)} = \frac{4\pi.r.(h-1).\sin 2\phi.\cos\varepsilon}{(h+1).\sin(\phi-\varepsilon)}$$

After rearrangement to get the following:

$$\frac{1-k}{1+k} = \frac{C_l.b.l.\cos(\phi-\varepsilon)}{8\pi.r.\cos\varepsilon.\sin^2\phi} \quad (8)$$

$$\frac{h-1}{1+h} = \frac{C_l.b.l.\sin(\phi-\varepsilon)}{4\pi.r.\sin 2\phi.\cos\varepsilon} \quad (9)$$

The wind rotor is divided in to equal 10 sections and C_p value for each section was calculated by using the iterative procedure. The curve of coefficient of lift (C_l) and of coefficient of drag (C_d) verses the angle

of attack (α) of the blade profile NACA 4415 was used for this calculation [2]. Then, coefficient of performance of the wind rotor segment at radius r (C_{pr}) with respect to different tip speed ratios (λ_0) was calculated.

$$C_{\Pr} = \frac{dP_u}{\rho.\pi.r.dr.V^3} = \lambda^2.(1+k).(h-1) \quad (10)$$

$$P = \int_r^R C_{\Pr}.\rho.\pi.r.dr.V_1^3 = \tfrac{1}{2}.C_p.\rho.\pi.R^2.V_1^3 \quad (11)$$

Then, coefficient of performance of the wind rotor (C_p) is given by,

$$C_p = \frac{2}{R^2}.\int_r^R C_{\Pr}.r.dr \quad (12)$$

Coefficient of momentum of rotor (C_m) is defined by,

$$C_m = C_p / \lambda_0 \quad (13)$$

Table 2: Theoretically calculated performance of the wind rotor

Tip-Speed Ratio (λ_0)	Cp	Cm
0	0.00	
1	0.04	0.04
2	0.12	0.06
3	0.21	0.07
4	0.30	0.08
5	0.37	0.07
6	0.40	0.07
7	0.39	0.06
8	0.34	0.04
9	0.25	0.03
10	0.13	0.01
11	0.00	0.00

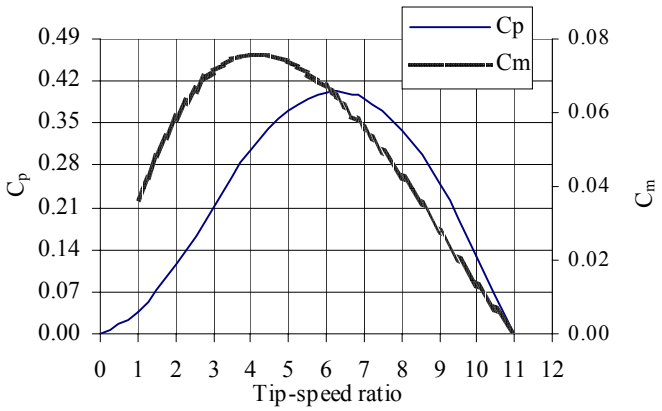

Figure 3: Performance curve of the existing NERDC wind-rotor

3. CHARACTERISTICS OF PERMANENT MAGNET GENERATOR

In this wind-turbine-battery-charging unit, the wind-rotor is directly coupled to the permanent magnet generator. Power absorption by the permanent magnet generator at different rotational speed is found by using a torque meter. The load for the generator is a bank of 12V-batteries and the prime mover is an induction motor driven by a variable-frequency inverter. Characteristic performance of the permanent magnet generator is presented in table 3 and figure 4 [3].

Table 3: Characteristic performance of permanent-magnet generator (PMG) with 12V battery bank

Speed (rev/min)	Torque(N.m)	Power input (W)	Power output (W)	Efficiency %
200	2.59	52.1	0.6	1.2
225	2.7	63.9	3.8	5.9
250	3.2	82.9	10.2	12.2
275	3.4	97.7	19.7	20.2
300	4.0	127.9	35.2	27.5
325	4.5	154.0	42.6	27.6
350	4.7	174.1	55.8	32.0
375	4.9	195.5	67.4	34.5
400	5.6	236.9	82.1	34.6
425	6.5	292.0	92.6	31.7
450	6.8	319.8	106.2	33.2
475	7.0	348.9	118.5	33.9
500	7.5	390.9	129.5	33.1
525	7.9	435.7	140.2	32.3
550	8.4	482.2	149.4	30.9
575	8.6	517.7	162.2	31.3
600	8.6	540.2	169.3	31.3

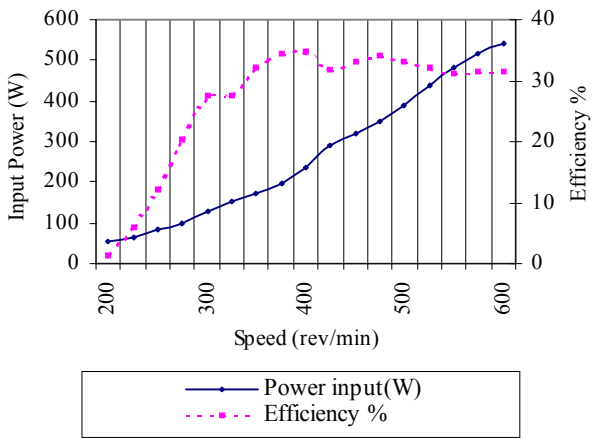

Figure 4: Characteristic performance of permanent-magnet generator

Figure 5: NERDC permanent magnet generator

4. COMBINED PERFORMANCE OF THE WIND ROTOR AND THE PERMANENT MAGNET GENERATOR

By considering the curve of C_p versus λ_o of the wind rotor, the power output of the wind rotor corresponding to each wind speed can be found out. Then, the generator and the rotor performance curves of the wind turbine-generator system can be plotted, as shown in Figure 6.

$$\lambda_0 = \frac{\omega . r}{V_1} \qquad (13)$$

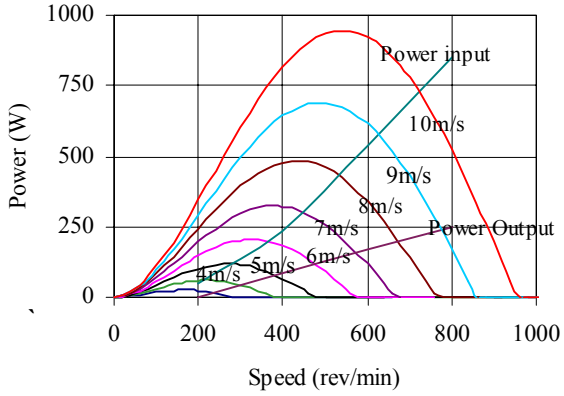

Figure 6: Generator and rotor performance curves of NERDC wind-turbine generator

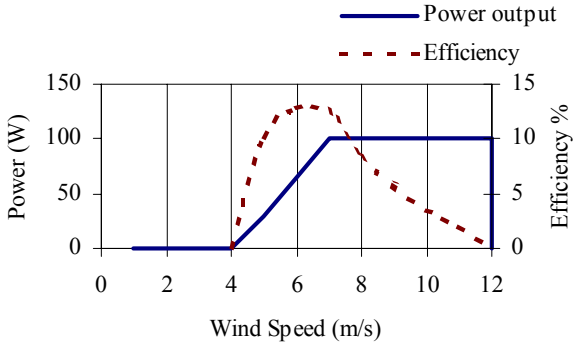

Figure 7: Output power characteristics and efficiency of NERDC wind turbine

The curve of power output verses rotational speed of the wind rotor at each wind speed and the curve of power input Vs rotational speed of the generator is plotted in the same graph. The generator power input curve should pass through the maximum points of the power output curves of wind-rotor at each wind speed, if they properly match.

5. CONCLUSION

By considering the combined characteristic graphs (Figure 6), it is evident that generator power input curve is not passing through the maximum points of the wind rotor characteristics curves. It means that the wind turbine-generator is not performing at the optimum condition. To match the wind-rotor and generator, these two should be coupled by using a suitable speed-increasing gearbox or the wind rotor or generator characteristic performance should be modified to tally each other. Power output characteristics of the wind turbine with this type of passive controlling design at wind speeds higher than the rated value are complex. The prediction of such characteristics is not a part of the present study. Therefore, it is assumed that the inclined-hinge tail-vane with side-vane mechanism works ideally such that the power output above the rated wind speed remains at 100W until the cut-off wind speed is reached. Variations of overall efficiency of the system together with the effect of power modulation can be observed in Figure 7.

ACKNOWLEDGMENTS

The authors wish to acknowledge the encouragement by Mr. Ranjan Rodrigo, Chairman of the National Engineering Research & Development Centre of Sri Lanka, to forward this paper to Tenth Asian Congress of Fluid Mechanics. We would like to thank Dr. Susil Weerarathne for his invaluable assistance to edit this paper.

REFERENCES

[1] Gourieres, D. Le. ***Wind Power Plants Theory and Design.*** Oxford: Pergamon press, 1982, 76-120.

[2] Abbott. Ira. H and Von Doenhoff. Albert. E. ***Theory of Wing Section***, 1958. 412 and 490-491.

[3] Wimalarathne, G. B. Report on Design of a Low Speed Generator for Micro Scale Power Generation. NERD Centre of Sri Lanka, Ekala, Ja-Ela, Sri Lanka, 1994.

Proceeding of the Tenth Asian Congress of the Fluid Mechanics
May, 17-21, 2004, Peradeniya Sri Lanka

USING SYMBOLIC CALCULATION FOR SOLVING LAMNAR FLOW THROUGH A LOOSLEY CURVED PIPE

Kamyar Mansour
(Department of Aerospace Engineering, Amirkabir University of Technology, Tehran , Iran, 15875-4413
and
Flow Research and Engineering, P.O. Box 8184, Palo Alto, CA, 94305)
mansour@aut.ac.ir

ABSTRACT In this paper we consider fully developed steady laminar flow through a toroidal pipe of small curvature ratios. The solution is expanded by computer in powers of Dean number. and the series extended by means of symbolic calculation up to 18 terms. Analysis of these expansions allows the exact computation for arbitrarily accuracy up to 50000 figures. Although the range of exactness is almost the same order of the radius of convergence but Pade approximation lead our result to be good even for higher value of the Dean number.

---

1. INTRODUCTION

We adopt Dean's co-ordinate system(r, θ) reference [1] and his normalization: Lengths are referred to the radius a of the pipe, and the velocity w down the pipe to the maximum speed W_0=Ga^2/4μ in a straight pipe under the same axial pressure gradient G=$L^{-1}\,\partial p/\partial\phi$ but the stream function ψ for the secondary motion is referred to kinematics viscosity ν (which mean that transverse velocities are referred to ν /a). then in the approximations of negligible helicity and loose coiling the Navier-Stokes equations for incompressible fluid reduce to(dean' equation (15)-(18) reference [1])

$$\nabla^2 W + 4 = \frac{1}{r}\left(-\frac{\partial\psi}{\partial\theta}\frac{\partial W}{\partial r}+\frac{\partial\psi}{\partial r}\frac{\partial W}{\partial\theta}\right) \tag{1}$$

$$\nabla^4\psi + KW\left(\cos\theta\frac{\partial W}{\partial r}-\frac{\sin\theta}{r}\frac{\partial W}{\partial\theta}\right)=\frac{1}{r}\left(-\frac{\partial\psi}{\partial\theta}\frac{\partial}{\partial r}+\frac{\partial\psi}{\partial r}\frac{\partial}{\partial\theta}\right)\nabla^2\psi \tag{2}$$

$$W=\psi=\frac{\partial\psi}{\partial r}=0 \quad \text{at} \quad r=1 \tag{3}$$

where

$$\nabla^2=\frac{\partial^2}{\partial r^2}+\frac{1}{r}\left(\frac{\partial}{\partial r}\right)+\frac{1}{r^2}\left(\frac{\partial^2}{\partial\theta^2}\right)$$

$$K^2=2\left(\frac{W_0 a}{\nu}\right)^2\frac{a}{L}=\frac{G^2a^7}{8\mu^2\nu^2L}$$

$$W=\psi=\frac{\partial\psi}{\partial r}=0 \quad \textbf{At} \quad r=1$$

2. SERIES DERIVATION AND COMPUTER EXTENSION FOR SMALL CURVATURE, $a / L << 1$

If the pipe is straight that K is small, the nonlinear terms on the right hand side of equation (1) are negligible and the first approximation is linear:

$$W_1 = 1 - r^2 \tag{4}$$

As auther in [1] mentioned one can systematically improve on this approximation by expanding in Powers of K according to:

$$W = W_1 + (\frac{K}{576})W_2 + (\frac{K}{576})^2 W_3 + \cdots = \sum_{n=1}^{\infty} W_n (\frac{K}{576})^{n-1} \tag{5}$$

$$\psi = \psi_1 (\frac{K}{576}) + (\frac{K}{576})^2 \psi_2 + (\frac{K}{576})^3 \psi_3 + \cdots = \sum_{n=1}^{\infty} \psi_n (\frac{K}{576})^n \tag{6}$$

By plugging (5),(6) in to equations (1) and (2) and equating like powers of K one obtains:
:

$$\psi_1 = \left(4r - 9r^3 + 6r^5 - r^7\right)\sin(\theta)$$

$$\psi_2 = \left(\frac{4979r^2}{5600} - \frac{255r^4}{112} + \frac{81r^6}{40} - \frac{4r^8}{5} + \frac{3r^{10}}{16} - \frac{9r^{12}}{350} + \frac{r^{14}}{1120}\right)\sin(2\theta)$$

$$\psi_3 = \left(-\frac{114834261\mathrm{r}}{172480000} + \frac{678826429\mathrm{r}^3}{310464000} - \frac{76529\mathrm{r}^5}{23520} + \frac{3038603\mathrm{r}^7}{940800} - \frac{538211\mathrm{r}^9}{224000} + \frac{286821\mathrm{r}^{11}}{224000} - \frac{107\mathrm{r}^{13}}{224} + \frac{37953\mathrm{r}^{15}}{313600} - \frac{12211\mathrm{r}^{17}}{627200} + \frac{16301\mathrm{r}^{19}}{9408000} - \frac{24209\mathrm{r}^{21}}{388080000}\right)\sin(\theta) + \left(\frac{118164521\mathrm{r}^3}{931392000} - \frac{47753r^5}{140800} + \frac{6533r^7}{19600} - \frac{1819r^9}{10500} + \frac{5829r^{11}}{78400} - \frac{1293r^{13}}{44800} + \frac{3233r^{15}}{403200} - \frac{1121r^{17}}{784000} + \frac{4759r^{19}}{34496000} - \frac{1207r^{21}}{186278400}\right)\sin(3\theta)$$

$$W(1) = \left(\frac{19r}{40} - r^3 + \frac{3r^5}{4} - \frac{r^7}{4} + \frac{r^9}{40}\right)\cos(\theta)$$

$$W_2 = -\frac{4119}{44800} + \frac{19r^2}{40} - \frac{331r^4}{320} + \frac{99r^6}{80} - \frac{569r^8}{640} + \frac{157r^{10}}{400} - \frac{33r^{12}}{320} + \frac{r^{14}}{70} - \frac{r^{16}}{1280} + \left(\frac{14569r^2}{141120} - \frac{2297r^4}{8400} + \frac{1317r^6}{4480} - \frac{139r^8}{800} + \frac{61r^{10}}{960} - \frac{87r^{12}}{5600} + \frac{47r^{14}}{22400} - \frac{r^{16}}{8820}\right)\cos(2\theta)$$

$$W_3 = \left(-\frac{9352505441\mathrm{r}}{45534720000} + \frac{5279537279\mathrm{r}^3}{6209280000} - \frac{6717174019\mathrm{r}^5}{3725568000} + \frac{28013023r^7}{11289600} - \frac{263825837\mathrm{r}^9}{112896000} + \frac{3469721r^{11}}{2240000} - \frac{163923r^{13}}{224000} + \frac{154149r^{15}}{627200} - \frac{2581931r^{17}}{45158400} + \frac{975431r^{19}}{112896000} - \frac{1549741r^{21}}{2069760000} + \frac{2849009r^{23}}{102453120000} \right) \cos(\theta)$$

$$\left(\frac{186219491\mathrm{r}^3}{13837824000} - \frac{107649071\mathrm{r}^5}{2483712000} + \frac{25543729\mathrm{r}^7}{413952000} - \frac{453907r^9}{8467200} + \frac{87119r^{11}}{2688000} - \frac{355863r^{13}}{25088000} + \frac{1177r^{15}}{268800} - \frac{53191r^{17}}{56448000} + \frac{2311r^{19}}{17248000} - \frac{82741r^{21}}{7451136000} + \frac{6113r^{23}}{16144128000} \right) \cos(3\theta)$$

We have found 18 terms exactly by means of symbolic language (confirmed by numerical calculation of Vandyke [2]), however for saving space only we report the result for the Flux ratio as defined as the ratio of the flux F_c through a loosely curved pipe to the flux F_s through a stationary pipe with the same pressure gradient. Its series has the form:

$$\frac{F_c}{F_s} = \sum_0^\infty a_n \left(\frac{K}{576} \right)^{2n} = 1 - \frac{1541}{50400}\left(\frac{K}{576} \right)^2 + \frac{6471982981}{542442700800}\left(\frac{K}{576} \right)^4 - \frac{80321152554888274264316429}{12198321972347948236800000000}\left(\frac{K}{576} \right)^6 + \frac{8487262921087293926345986837165640639113}{2002421783056432738234386087936000000000000}\left(\frac{K}{576} \right)^8 - .... \quad (7)$$

$$\left(\frac{F_r}{F_s} \right)^{-1} = \sum_0^\infty b_n \left(\frac{K}{576} \right)^{2n} = 1 + \frac{1541}{50400}\left(\frac{K}{576} \right)^2 + ... \quad (8)$$

3. ANALYSIS OF SERIES AND DISCUSSION

Pade approximants has been used in original forms to enable us to increase the range of applicability of the series as has been used in the works of Mansour [4] and Mansour[3]. This method does not necessarily require any information about the radius of convergence. The Pade approximants provide an approximation that is invariant under an Euler transformation of the independent variables. The theory of Pade approximants has been used extensively in Mansour [4]. Briefly stated, the Pade approximant is the ratio P(K)/Q(K) of polynomials P and Q of degree m and n, respectively, that, when expanded, agrees with the given series through terms of degree m+n, and normalized by P(Q)=1. Such rational fractions are known to have remarkable properties of analytic continuation. The coefficients of the power series must be known to degree m+n. By equating like power of g(x) and P(K)/Q(K), the linear system of m+n+1 equation must be solved to obtain the coefficients in the functional form P(K)/Q(K).Pade approximation of orders [0/1], [1/2] are respectively:

$$\frac{\frac{1541}{50400}-\frac{14573594666408994098479553949921210960213647K}{10032400561105691555252412741894212762880000000}}{1+\frac{10300437498675992465037432964019932265281891K}{11903522887978578472303457975501466730560000}+\frac{34239117785914733549166549737392061857165170555623502 1K^2}{27993054252165732878072105644804643109513080094720000 00}}$$

$$\frac{1541}{50400(1+\frac{6471982981K}{16585400832})}$$

When we form the ratios [0/1], [1/2], [2/3],[3/4] and [4/5] of the Pade approximants, It can be shown , they agreed up to the value $K \cong 1300$ (k=1.35). White [5] introduced $k^2 = 2(\frac{W_m a}{\nu})^2 \frac{a}{L}$ which is based on the actual mean velocity W_m down the pipe. This conclusion is confirmed as is plotted from the ratios [0/1] and [4/5] versus k in Figure 1.

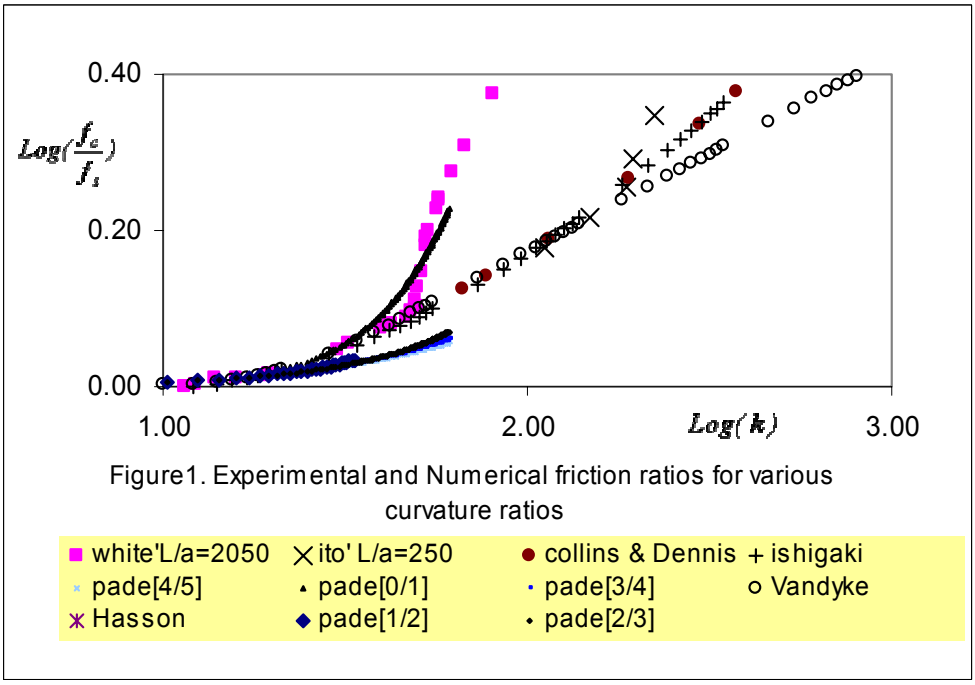

Figure1. Experimental and Numerical friction ratios for various curvature ratios

4. CONCLUSION

This work is concerned with the problem of flow through a loosely coiled pipe .In this problem, then by using symbolic language like MACSYMA we have fund some terms of their corresponding Stokes expansion. we then obtained 16 terms exactly by means of symbolic calculations and agreed with the values given by work of Vandyke [2] up to 16th figure of accuracy. Then we tried to make analytic continuation by using Pade approximation. By doing so, we are successful to increase the range of the

validity of the series from zero up to $K \cong 1300$ (The radius of convergence is about 584 as was found accurately by Vandyke [2]) and our results are exact calculations up to arbitrarily figure of accuracy . In other words, we have solved the nonlinear partial differential equation exactly by means of computer and that is a real success. .

A major difference between series extension method Vandyke [2] and those of other analyses is in the asymptotic behavior of the friction factor as the Dean number K and hence k increases. The prevailing opinion has been that the relationship goes as $f_r / f_s \sim k^{1/2}$ (supported by numerical works of [6] and [7]), whereas Vandyke [2] found that $f_r / f_s \sim k^{1/4}$ Ramshankar & Sreenivasan [8]] for this curved pipe problem tried to make fine experiment to match the series extension would have to satisfy that is the flow to be fully developed at high Dean number namely bigger than 500 and laminar a/L less than .03. But his result adds another mystery to this paradox and they obtained data, which lay closer to the series extension method than. the previous experiments of [5],[9],[10].

As Vandyke[2] has found the friction ratio grows eventually as the 1/4 power of the practical Dean number based on the actual mean flow speed down the pipe, rather than the 1/2power predicted by four different approximate boundary layer models Adler [11] collision of two layers and Ito [12], Mori & Nakayama[13], Smith[14], Dennis&Riley [15] suppress it and Barua[16] believes on separation Vandyke[17] in this article put the whole thing as an paradox. Jayanti&Hewitt[18] has gone further even questioned the result obtained by Vandyke[2] . These controversial results made us to do exact calculation in this article and we hope first attempt for exact calculation of much higher Dean number.

REFRENCE

[1] Dean, W.R. 1927 Note on the motion of fluid in a curved pipe. Phil. Mag. (7) 4,208-223

[2]Van Dyke, M. 1978 Extended stokes series: laminar flow through a loosely coiled pipe. J.Fluid Mech.,86, 129-145

[3] Mansour, K. 1985 Laminar flow through a slowly rotating straight pipe. J. Fluid Mech. 150, 1-24.

[4] Mansour, K. 1993 Using Stokes Expansion For Natural Convection inside a two-dimensional cavity. Fluid Dynamics Research, 1-33

[5]White, C. M. 1929 Streamline flow through curved pipes. Proc. Roy. Soc. A 123, 845-663.

[6]Collins, W. M. &Dennis, S. C. R. 1975 The steady motion of a viscous fluid in a curved tube.Quart. J. Mech. Appl. Maths. 28, 133-156

[7]Ishigaki, H. "Analogy between laminar flows in curved pipes and orthogonal rotating pipes". J. Fluid Mech. (1994), vol.268, pp. 133-145

[8]Ramshankar, R. & Sreenvasan, K. R. 1988 A paradox concerning the extended Stokes series solution for the pressure drop in coiled pipes. Phys. Fluids, 1339-1347.

[9]Hasson,D. 1955 “Streamline flow resistence in coils. Research 8(1) supplement p.S1

[10] Ito, H.,1959 Friction factors for turbulent flow in curved pipes.
Trans.ASMEJ.BasicEngng.81,123-134

[11]Adler,M.”Flow in curved tubes” Z.Angew.Math.1934 Mech.,14,257

[12] Ito, H., 1969 Laminar Flow in curved pipes Z. agnew. Math. Mech. 11. 653-663

[13] Mori, Y. & Nakayama, W. 1965 study on forced convective heat transfer in curved pipes (1st report, laminar region). Intl. J. of Heat Mass Transfer 8, 67-82

[14]Smith, F. T. 1976 Steady motion within a curved pipe. Proc. Roy. Soc. A 347, 345-370

[15]Dennis,S.C.R. and Riley,N. 1993 "On the fully developed flow in a curved pipe at large Dean number" Proc. Roy. Soc. A.434,473-478

[16]Barua,S.N. 1963 On secondary flow in stationary curved pipes. Quart. J. Mech. Appl. Maths. 26. 61-77

[17]Van Dyke, M. 1989 some paradoxes in viscous flow theory. "Some unanswered question in fluid mechanics " (ed. L. M. Trefethan & R. L. Panton).Appl. Mech. Rev. 43, 153-170

[18] Jayanti ,S & Hewitt.G.F "On the paradox concerning friction factor ratio in laminar flow in coils", Proc. R. Soc. Lond. A (1991) 432, 291-299

Proceedings of the Tenth Asian Congress of Fluid Mechanics
17-21 May 2004. Peradeniya. Sri Lankn

THE AERODYNAMIC PERFORMANCE ANALYSIS OF A HIGH SPEED TRAIN

Hongqi TIAN
Key Laboratory of Train Safety, Central South University, Changsha, Hunan, China, 410075

ABSTRACT: With the running speed of trains raised, the air resistance sharply increased, and energy was over-consumed; at the same time a larger aerodynamic lift occurred, which resulted in the "floating" of the train and consequant derailment. A greater aerodynamic lateral force also occurred, which affected the lateral stability of train. In this paper, on the basis of the numerical computation, wind tunnel tests, moving model tests, and full-scale train test results, an analysis was carried out on the effect of the nose shapes of the train to the air resistance, lift and lateral force on the high-speed train. The research shows that the train with single arch nose is slightly better than a double arch in decreasing aerodynamic resistance; the absolute value of resistance and lift force on the train with bottom cover are far less than that with skirt plate. The train with the double arch nose, however, is slightly better than the single arch in reducing aerodynamic lateral forces; and the position at which the lateral force acts on the double arch nose train is lower than that for the single arch nose train, so that the former has better lateral stability.

1 INTRODUCTION

The train is a large long object running on ground at high speed; a series train aerodynamic problems exist, which are different from those in airplanes and aerospace. There are some special problems that affect train aerodynamic performance in China`s high-speed railway, such as two trains passing by each other, ground effect, and complicated environment. Therefore, in the developing the High Speed Train, studies such as train aerodynamic numerical computation, wind tunnel tests, moving model tests and theory analysis should be carried out. The following aspects had been studied: train aerodynamic resistance and air lift, horizontal air force, train surface pressure distribution, air pressure pulse from two trains passing by each other and flow field around train.

There are two types train nose shape in the train design. One is the single arch where, except from bottom flow guide plate, the largest outline of head longitudinal section is a protruding streamline shape. The other is the double arch where the largest outline of the head longitudinal section is formed as two segments of protruding shape and one segment of concaving shape linking the other two segments.

There are three bush the bottom shapes for the head, the trailer and the end car. In the first shape, a mantle covers the bogies two sides and the car bottom, which make the car body bottom slick (except the bottom of the bogies); this kind of structure is simply called car bottom mantle structure. In the second one, between bogies and on the truck side frame, the outside baffle-like skirt is fixed on the girder border; then the bottom equipment is confined between two skirt baffles; this structure is called bottom skirt baffle structure. The third structure has no car bottom mantle or bottom skirt baffle; all the equipment is under the bottom of the car body and exposed to open air.

2 AIR PRESSURE PULSE FROM TWO TRAINS PASSING BY EACH OTHER

The air pressure pulse is an aerodynamic problem that exists only in high-speed railway transportation, but not in the airplane, aerospace and highway transportation. It is a transient load due to pressure impact; its negative and positive peak values appear within about several tens of milliseconds. The factors which affect the air pressure pulse are mainly: the train speed, track interval, car body width, boundary layer thickness, train shape(include nose shape and car body section outline and train configuration. The peak value seriously affects high-speed railway safety, passenger comfort level, and project investment for building and maintaining railway lines.

2.1 The Influence of Head Shape to Air Pressure Pulse from Two Trains Passing by Each Other

The outcome of moving model tests showed that the air pressure pulse from two trains passing by each other are almost equal for double arch and single arch nose. for equal velocity of the two trains passing by each other, the air pressure pulse of the double arch nose train is a little smaller then the single arch nose.

According to the numerical computation and full-scale tests, the length of the train head has a large influence on the air pressure pulse from two trains passing by each other. The longer the train head, the smaller the volume of the air pressure pulse.

2.2 The Analysis of Air Pressure Pulse Endure by Power Train Windows

According to the numerical computation and full-scale test, when high speed train running at a speed of 280 km/h passing by another train running at 200 km/h, air pressure pulses of 611 Pa and 780 Pa occur separately on the high speed train head locomotive windows and end locomotive windows; while those of flank windows are 706 Pa and 883 Pa. The reason why the air pressure pulses differ is mainly because along the length of the train, the boundary layer becomes thicker, the effective space between the passing trains becomes smaller, and thus the air pressure pulse amplitude is larger. Also, under the influence of train boundary layer, the front windows and side windows of end locomotive driver room endure a larger air pressure pulse than the windows of head locomotive driver room.

2.3 Pressure Changes in the Carriages

From data measured by the pressure sensor fixed in the carriages, pressure in the carriages changes not only with the carriage airproof performance but also with the tiny distortions of train window because of the pressure change outside.

3 TRAIN AERODYNAMIC RESISTANCE

As train speed increases, air resistance becomes the main resistance for the running train. In China, when traditional trains with blunt head run at 120 km/h, air resistance occupies about 40％; When the speed-improving train runs at 160km/h, this percentage rises to 70％. Therefore, experts on train aerodynamics in the world are searching for measures to reduce the air resistance to reduce energy consumption. The factors affecting air resistance of running trains are speed, shape (include the head and end part shape, the car body configuration, the figure of every part), train surface lubricity level, etc. Research results on air resistance are listed in table 1.

Table 1: Air resistance of the train (without crosswind)

Head type	Resistance Coefficient (Cx)				Train aerodynamic resistance (N)	Car body shape
	Head car	Trail car	End car	The train formed of 2 locomotive and 9 vehicles		
Train with single arch nose	0.211	0.08	0.251	1.182	$0.61.V_s^2$	Car bottom mantle structure
	0.232	0.121	0.279	1.6	$0.825.V_s^2$	Car bottom skirt baffle structure
	0.305	0.162	0.376	2.139	$1.103.V_s^2$	Car bottom without mantle & skirt
Train with double arch nose	0.22	0.086	0.24	1.234	$0.636.V_s^2$	Car bottom mantle structure
	0.242	0.129	0.266	1.669	$0.861.V_s^2$	Car bottom skirt baffle structure
	0.318	0.164	0.359	2.153	$1.11.V_s^2$	Car bottom without mantle & skirt

3.1 Compare of Double Arch With Single Arch Nose

Under every combinatorial state, air resistance of the front car for the single arch nose is slightly smaller than that for the double arch nose. As the single and double arch nose shape affect car body air flow in different ways, the aerodynamic resistance on the trailer of double arch nose train is slightly smaller than that for the single arch. The aerodynamic resistance of end car, single arch is, however, a little larger than for the double arch. When head and end cars have the same nose shape, the aerodynamic resistances are almost equal, with the resistance of the single arch nose train a little smaller.

3.2 Effect of Bottom Shape on Aerodynamic Resistance

Comparison of the effects of car bottom mantle structure, car bottom skirt baffle structure, and the structure without mantle & skirt, we find that with the car bottom adopting the skirt baffle structure, instead of the car without mantle & skirt structure, the aerodynamic resistance of the head car reduces by 24 percent, the middle car by 25 percent, the end car by 26 percent, and the full train by 25 percent. When the bottom of the car body has the mantle structure, is compared to that without mantle & skirt, the aerodynamic resistance of the head car reduces by 31 percent, the middle car by 51 percent, the end car by 33 percent, and the full train by 45 percent. When the head and end car bottom with skirt baffle structure, and the trailer bottom with a mantle structure, is compared to that without mantle & skirt structure, the full train aerodynamic resistance reduces by 37 percent. Thus in order to reduce the resistance, the bottom of the car should append covering.

3.3 The Influence of Crosswind

When crosswind exists, the head, the end car and the trailer endure the larger resistance. Compared with the condition without crosswind, when crosswind speed is 15m/s and train speed is 270 km/h, the aerodynamic resistance of the head car increases by about 14%, the trailer, by about 46%, the end car, by about 20%, and the full train, by about 38%. When crosswind speed is 25 m/s and train speed is 200 km/h,

the aerodynamic resistance of the head car increases by about 13%, the trailer, by about 68.3%, and the end car, by about 38%, to the full train, by about 60%. Thus, crosswind has a strong influence on aerodynamic resistance.

4 TRAIN SURFACE PRESSURE DISTRIBUTION

In order to improve passenger comfort level, wind exiting and inhaling locations for air conditioning and cooling system and air exchanging system must be rightly selected. The selecting srules are: wind inhaling location should be arranged in positive pressure area; wind exiting location, in the negative pressure area. Otherwise, the air conditioner cannot draw fresh air as the train surface has negative pressure, and cooling water would flow into carriages due to the positive pressure. In addition, from the train surface pressure distribution, we can apply the flow mechanism of flow field around train to improve the train aerodynamic performance. Train surface pressure distribution is affected by the speed, shape and environment around train.

(1) With train speed above 180 km/h, the flow state enters the self-simulating region, as the surface pressure coefficient has no relationship to speed (it becom constant), while the absolute pressure coefficient for the carriages shows a moderate rise in the speed.

(2) The surface pressures at the end walls are all positive; and the pressure values in the wind direction and opposite to wind direction are nearly the same. On the end walls, pressure distribution is uniform and stable so that they are the ideal locations for air conditioner air intake.

(3) With the exception of the end wall, the pressure of all car body surfaces is negative, and all points in any section have almost the same pressure. But, at the bottom of car body and around the transition arc, the negative pressure is a little larger when train speed is 270 km/h, it is about 390 Pa, where it will be of help to exit the wind of air condition equipment..

5 TRAIN AIR LIFT

The absolute value of train air lift rises as the square of the speed. In the high speed train, which belongs to the wheel-rail system, if positive lift is excessively large, the wheel-rail contact load will reduce, causing the train to be lifted and possible derailment; but if negative lift is excessively large, the dynamic axle load will rise to produce greater impact from train to rail. Because air lift is mainly determined by train shape, in order to obtain the excellent running performance, the train air lift should be chose to zero as much as possible in the design of the train shape. The research results on train air lift are listed in table 2:

(1) Comparing between the single and double arch nose, for air lift, the single arch nose is a little better than the double one when without crosswind; but with crosswind exists, the double arch nose is slightly better than the single arch. As a result, the single and double arch nose have similar performance on air lift.

(2) Comparing of bottom shapes. Without crosswind, the air lift of the front car bottom with mantle structure is less than or near to zero, but with skirt baffle structure, the absolute value of air lift would rise. For the trailer, with mantle structure, the air lift will be below zero; but with skirt baffle structure, the value will be above zero. At the same time, when the end car bottom has a mantle structure, the air lift will be far lower than that of the skirt baffle structure produced. In general, the absolute value of air lift

with mantle structure is far lower than skirt baffle structure does.

Table 2: The train air lift (KN)

Head type	Train speed：270km/h Crosswind speed：0 m/s			Train speed：270km/h Crosswind speed：15m/s			Train speed：200km/h Crosswind speed：25m/s			Car body shape
	Head car	Trail car	End car	Head car	Trail car	End car	Head car	Trail car	End car	
Train with single arch nose	-2.368	-1.353	6.09	19.736	28.232	21.879	34.632	29.290	25.371	Car bottom mantle structure
	-2.842	1.241	8.346	22.819	35.562	23.307	37.582	35.684	27.434	Car bottom skirt baffle structure
Train with double arch nose	-2.444	-1.316	6.353	18.082	28.232	22.856	31.662	29.496	25.577	Car bottom mantle structure
	-2.932	1.241	8.721	20.901	35.562	24.322	34.137	35.891	27.434	Car bottom skirt baffle structure

(3) With crosswind, the head, the end car and the trailer are all have larger positive air lift than that without crosswind. With a crosswind speed of 15 m/s, and a train speed of 270 km/h, the aerodynamic lift of the head car rises to about 9 times, that for the trailer, to about 20 times, the end car, to about 3 times; if the crosswind speed is 25 m/s, and the train speed is 200km/h, the head car aerodynamic lift rises to about 12 times. So, the crosswind has serious effects on the magnitude of air lift.

6 TRAIN TRANSVERSE AIR FORCE

The train running direction is rarely parallel to the environmental wind direction, so, in the windy environment, the train wind and the environment wind can be added to be one wind, acting on the vehicle at an angle. Also because the aweather and dead wind side of the vehicle will produce a non-symmetry air flow, this will produce a transverse force. The magnitude and its point of acting of the resultant force (this is also the pressure center) is determined by environment wind speed and direction, the vehicle shape and size. The location of acting of the transverse force is not the center gravity of vehicle, and is usually above the rail surface. If the location is nearer to rail surface, the lateral roll moment of the vehicle will be smaller, and the vehicle transverse stability will become better.

Based on the wind tunnel test results, we may compare the single and double arch noses. For head car, the transverse force values are almost the same, but the transverse force of the train with double arch nose has a lower point of action, thus, the train with double arch head car has better transverse stability. For the trailer, the single arch nose train and the double arch nose train have similar transverse force values and acting location, so that the nose shape has little influence on the trailer transverse force and acting location. For the whole train, the double arch is slightly better than the single arch.

7 CONCLUSIONS

(1) The longer the streamline length of train head, the less will be the air pressure pulse from two trains passing each other, and the aerodynamic resistance. This will improve the aerodynamic performance of train.

(2) The air pressure pulse of the double arch nose train is less than the single arch nose train, but the aerodynamic resistance is greater than the single arch nose train, and air lift is nearly equal to the single arch nose train, while its transverse stability is better than the single arch nose train.

(3) Crosswind has a strong influence on aerodynamic resistance and lift.

(4) The end walls of the trailer and the drive car have a positive pressure, and hence the end walls are the ideal locations for the air condition wind inhaling.

(5) The bottom of car body and around the transition round arc have negative pressure, and are suitable locations for the wind exiting of air condition.

REFERENCES

[1] Y. Khandhia, CFD Simulation of Three Dimensional Unsteady Train Aerodynamics，Vehicle Aerodynamics，1996.10.

[2] 田红旗，贺德馨，列车交会压力波三维数值计算,铁道学报,2001.3

[3] 田红旗、卢执中，200km/h 电动旅客列车组控制车风洞试验研究，铁道车辆，1997.7

[4] 井门敦志等.列车先头部、后尾波形状最适化のための风洞试验.铁道综研报告.1993.7.

[5] P.A. Mackrodt，J.Steinheuer und G.Stoffers，Entwicklung Aerodynamisch Optimaler Farmen für das Rad/Schiene-Versuchsfahrzeng Ⅱ，AET(35)-1980